Research Article | Open Access

Microstructures

Eun et al. Microstructures 2026, 6, 2026065 DOI:10.20517/microstructures.2025.120

Interface-engineered Bi_2Te_3 powders via atomic layer deposited TiO_2-ZnO multilayer for improved thermoelectric performance

Su Min Eun[1], Eui Seon Lee[1], Jin Kyeong Shin[1], Sung-Tag Oh[1,2], Byung Joon Choi[1,2]

Keywords:
Thermoelectrics, atomic layer deposition, interface engineering, multilayer

Citation: Eun, S. M.; Lee, E. S.; Shin, J. K.; Oh, S. T.; Choi, B. J. Interface-engineered Bi_2Te_3 powders via atomic layer deposited TiO_2-ZnO multilayer for improved thermoelectric performance. *Microstructures* **2026**, *6*, 2026065. https://dx.doi.org/10.20517/microstructures.2025.120

Received: 9 Aug 2025
First Decision: 19 Sep 2025
Revised: 3 Oct 2025
Accepted: 30 Oct 2025
Published: 15 May 2026

Academic Editor:
Jing-Feng Li
Copy Editor:
Ping Zhang
Production Editor:
Ping Zhang

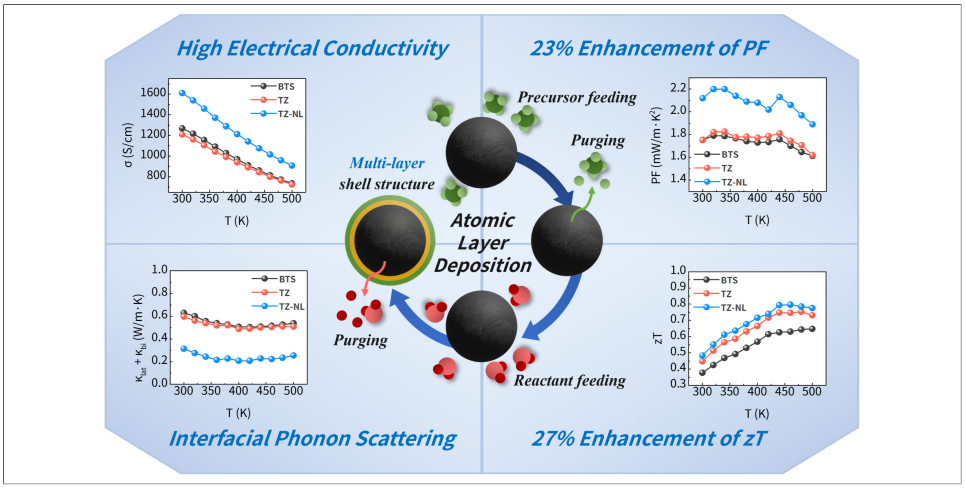

Abstract

Tailoring the interfacial properties at the nanoscale is essential for improving the performance of thermoelectric materials, where the simultaneous optimization of electronic and phononic transport remains a key challenge. We used atomic layer deposition (ALD) to conformally coat $Bi_2Te_3Se_{0.3}$ (BTS) powders with TiO_2-ZnO multilayer oxides. Two configurations were fabricated: ZnO/TiO_2 bilayers (2 nm thick) and $ZnO/TiO_2/ZnO/TiO_2$ multilayers (1 nm thick). The coated powders were consolidated by spark plasma sintering (SPS). The ALD-grown multilayers uniformly coated the powder and remained highly dense after sintering. Consequently, the multilayer-coated structure showed improved carrier concentration and mobility owing to interfacial electron donation and diffusion doping, enhancing electrical conductivity. Their high-density and continuous layers effectively reduce lattice thermal conductivity, resulting in a zT of 0.8 at 460 K, a 27% increase over uncoated BTS. The controlled interface design enabled effective tuning of both charge carrier and phonon transport. This study demonstrates that conformal interfacial engineering via ALD is a promising strategy for enhancing thermoelectric performance by simultaneously tuning the electronic and phononic transport properties

[1]Department of Materials Science and Engineering, Seoul National University of Science and Technology, Seoul 01811, Republic of Korea.
[2]The Institute of Powder Technology, Seoul National University of Science and Technology, Seoul 01811, Republic of Korea.

Correspondence to: Prof./Dr. Byung Joon Choi, Department of Materials Science and Engineering, Seoul National University of Science and Technology, Seoul 01811, Republic of Korea. E-mail: bjchoi@seoultech.ac.kr

through nanoscale interface design.

INTRODUCTION

In response to the growing importance of energy conservation and climate change mitigation, thermoelectric (TE) technology has emerged as an eco-friendly alternative energy source. TE technology can directly convert waste heat into electricity, addressing the major drawback of significant input-energy loss as waste heat in conventional renewable and carbon-based energy systems. Thus, TE technology holds great potential for application in diverse fields such as transportation, power generation, and industrial processes[1-3]. However, the low energy-conversion efficiency of current TE materials limits their practical applications; thus, continuous improvements through advanced materials and process engineering are required[4-7]. TE materials are classified as low- (300-500 K), mid- (500-900 K), and high-temperature (≥ 900 K) materials, and representative examples include Bi_2Te_3-, PbTe-, and SnSe-based alloys, oxides, two-dimensional materials, and superlattice-structured compounds. Bi_2Te_3 alloys exhibit excellent low-temperature TE properties owing to their layered crystal structure and van der Waals gaps along the c-axis, which suppress phonon transport, as well as their high atomic mass, which reduces phonon velocity[8-16]. However, n-type Bi_2Te_3 has been reported to face difficulties in performance enhancement compared to p-type because of the sensitivity of electron concentration to defect structures and the requirement for precise grain alignment to accommodate the strong anisotropy of TE properties[17]. Therefore, achieving high-performance n-type Bi_2Te_3 alloys requires comprehensive understanding and independent control of defect structures, microstructures, and nanoscale features.

The figure of merit (zT), a key metric of TE performance, is expressed as

$$zT = \frac{S_2 \cdot \sigma \cdot T}{\kappa} \tag{1}$$

where S, σ, and κ are the Seebeck coefficient, electrical conductivity, and thermal conductivity, respectively[18]. These parameters are all carrier concentration-dependent and exhibit inherent trade-offs, particularly between electrical and thermal conductivities, making their simultaneous optimization challenging. Since the 2000s, various strategies such as nanostructuring, defect and band engineering, and texturing have been explored to improve zT. In particular, conventional nanoparticle-dispersion using mechanical mixing and ball milling can effectively lower thermal conductivity by controlling particle size, volume fraction, and physical dispersion. However, these methods are often limited because the carrier concentration strongly constrains improvements in the Seebeck coefficient, and the electrical properties and band alignment of the dispersed particles are difficult to predict accurately[19]. In contrast, interfacial engineering is advantageous for simultaneously coordinating charge and heat transport through control not only of physical factors such as interface thickness, density, and lattice coherency but also of carrier concentration and band alignment. In this study, we focus on interfacial engineering to decouple electrical and thermal transports.

Atomic layer deposition (ALD) has recently gained attention as a precise interfacial-engineering tool for enhancing TE performance[20-24]. ALD is an advanced thin-film growth technique that alternately injects precursors and reactants to form ultrathin conformal films, even at low temperatures. It enables atomic-level thickness control and uniform coating on complex structures, such as powder surfaces, offering process flexibility for TE research[25]. Therefore, ALD-based interfacial engineering can effectively lower lattice thermal conductivity by inducing interfacial phonon scattering while precisely controlling carrier concentration[26-32]. It can also enhance the Seebeck coefficient through the energy filtering effect at heterogeneous interfaces[33-37]. This occurs when materials with different bandgaps form potential barriers that selectively scatter low-energy carriers. Because excessively thick or abundant interfaces can reduce

electrical conductivity, precise interface design is critical. Jung *et al.* employed a powder-specific ALD system with gas fluidization and a rotating reactor to coat Bi_2Te_3 powders with approximately 10 nm thick ZnO films, and investigated the TE performance differences depending on the reactor type[38]. Although powder agglomeration occurred because of the relatively high humidity during processing in the rotary reactor, improved TE properties were obtained after sintering because of the increased carrier concentration and mobility associated with the oxygen-related residual ions. In subsequent studies, ZnO coatings with 40 and 100 ALD cycles were deposited in a rotary reactor. A zT value of approximately 0.9 was achieved in pellets with 40-cycle films, revealing the impact of film thickness on TE performance[39]. While the ZnO films effectively improved the electrical conductivity, an increase in both the electrical and thermal conductivities with thicker films highlighted the need for additional strategies to independently control the thermal conductivity. This has introduced heterostructures or dual/multilayer designs that can better balance the tradeoffs between electrical and thermal conductivities[40-42]. He *et al.* applied ZnO/Al_2O_3 multilayer ALD to CuNi alloy powders based on metallic system and achieved an 128% enhancement of zT[37]. This demonstrated that multilayer coatings can effectively induce energy filtering and phonon scattering, but it did not completely overcome the reduction of electrical conductivity. Moreover, it fundamentally differs from the Bi_2Te_3-based system in charge-transport mechanism and band structure. This study extends the multilayer ALD strategy, previously demonstrated for metallic alloys, to a semiconducting TE material, aiming to achieve not only lattice thermal conductivity reduction but also enhanced electrical transport.

In this study, we systematically investigated how the TiO_2-ZnO multilayer configuration - film composition, individual thickness, and interface density - affects TE properties. Using a rotary-reactor-based powder ALD process, TiO_2-ZnO multilayers were deposited onto the surface of Bi_2Te_3-based powders, followed by densification via sintering. Reactor rotation during ALD promotes uniform deposition by agitating the powders. TiO_2, which has a band gap similar to that of ZnO, offers high thermal stability and may alleviate the high-temperature degradation of Bi_2Te_3. Its relatively high Seebeck coefficient and low thermal conductivity can also contribute to reducing net thermal conductivity, though its low electrical conductivity limits its standalone application as a TE material[43-46]. Conversely, ZnO has high carrier mobility and electrical conductivity, supporting improved power factor (PF, $S^2 \cdot \sigma$) and making it a strong candidate for high-performance TE modules[47,48]. While concerns remain regarding interface-induced conductivity loss in multilayers, integrating TiO_2 with ZnO is expected to compensate for these losses.

MATERIALS AND METHODS

Powder preparation and film growth via ALD

$Bi_2Te_3Se_{0.3}$ (BTS) thin flakes were pulverized using a planetary ball mill. ZrO_2 balls (10 mm in diameter) with a powder-to-ball weight ratio of 1:5 were used. The BTS powder was dry-milled at room temperature for 5 h, resulting in a particle size (D_{50}) of 1-4 μm immediately after grinding. The fabrication process for the samples, with variations in the thin-film structure and thicknesses of ZnO and TiO_2, is illustrated in Figure 1. ZnO-TiO_2 thin films were deposited on the milled powder surfaces by ALD using a rotary reactor (Atomic Shell, CN-1 Co., Korea). The rotary reactor continuously stirred the powder during deposition, ensuring uniform exposure to the precursors and leading to a conformal coating of the particle surface. The base and process pressures during ALD were maintained at 3×10^{-2} and 1.8 Torr, respectively. Diethylzinc (DEZ, Lake Material Co., Korea) and titanium isopropoxide (TTIP, I-CHEMS Co., Korea) were used as precursors for ZnO and TiO_2, respectively, with H_2O as the reactant. N_2 was used as the purge gas at a flow rate of 200 sccm. The DEZ and TTIP sources were maintained at room temperature and 70 °C, respectively, and their respective delivery lines were heated to 80 °C for DEZ, 80 °C for TTIP, and 100 °C for H_2O. The deposition temperature was set at 150 °C, with a reactor rotation speed of 30 rpm. Prior to deposition, a 30-min preheating step was performed by rotating the reactor with N_2 gas to ensure uniform heating of the powder. Two sample types were prepared: a TiO_2/ZnO (TZ) (bilayer) sample with alternating 2 nm thick TiO_2 and

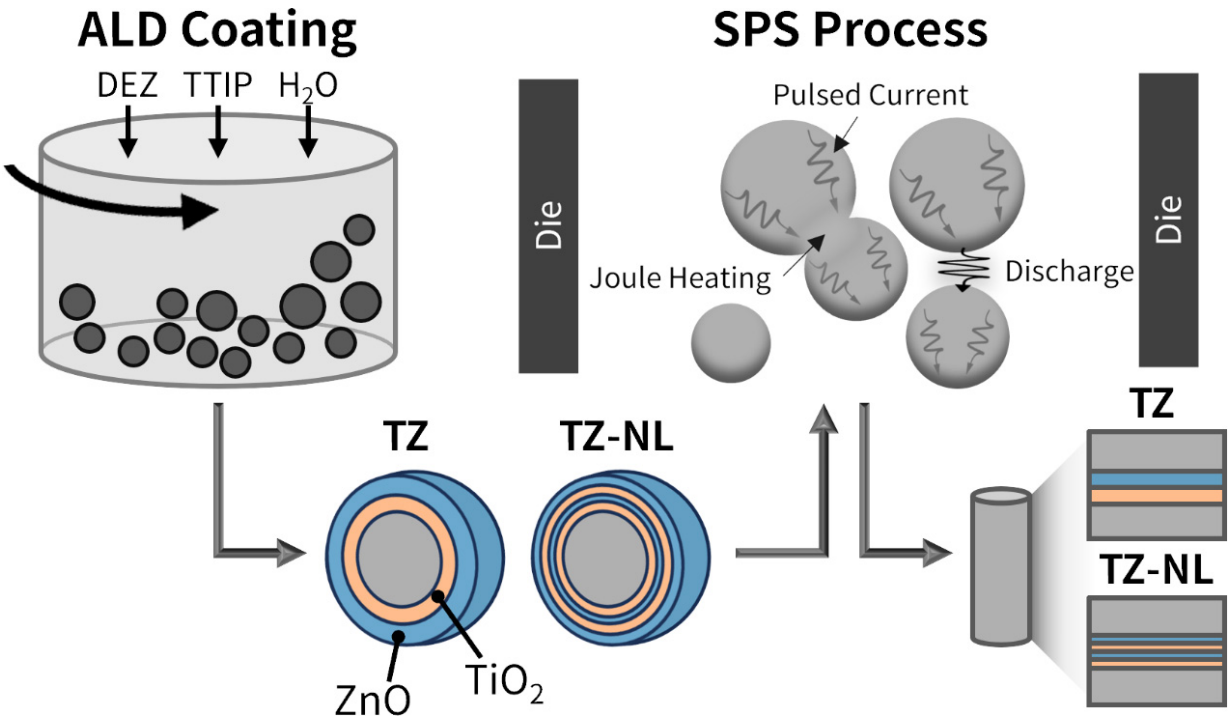

Figure 1. Sample preparation process flowchart. ALD: Atomic layer deposition; DEZ: diethylzinc; TTIP: titanium isopropoxide; SPS: spark plasma sintering; TZ-NL: TiO_2/ZnO nanolaminate.

ZnO layers, and a TZ-Nanolaminate (NL) (multilayer) sample with four alternating 1 nm TiO_2/ZnO layers. Each ALD batch contained 8 g of the powder. The number of ALD cycles was sophisticatedly controlled according to their growth-per-cycles (GPCs) of 0.1 nm/cycle for ZnO and 0.04 nm/cycle for TiO_2. The ALD cycle for ZnO was carried out as follows: DEZ injection (0.5 s) - N_2 purging (15 s) - H_2O injection (0.5 s) - N_2 purging (15 s), and for TiO_2: TTIP injection (1 s) - N_2 purging (30 s) - H_2O injection (1.5 s) - N_2 purging (30 s).

Consolidation via spark plasma sintering

After deposition, the coated powders were consolidated via spark plasma sintering (SPS; SPS-20, WELL TECH Co., Korea) at 673 K and 50 MPa for 5 min. The heating rate was 80 K/min, and the chamber pressure was maintained at 3.5×10^{-3} Torr. The SPS conditions were determined according to previous studies[38,39]. Graphite molds with a diameter of 15 mm and a height of 60 mm were used. After sintering, the samples were cooled while maintaining the applied pressure; the final pellet height was approximately 4 mm. The pellets were then polished using #200-#2000 sandpaper and cut using a diamond wire saw to prepare the specimens for the TE property measurements.

Material characterization

The particle size distributions before and after ALD were measured using a laser diffraction particle size analyzer (LS I3 320, BECKMAN COULTER, USA). The surfaces and fracture microstructures of the powders and sintered pellets were observed using high-resolution field-emission scanning electron microscopy (HR-FESEM; SUS8010, Hitachi, Japan), focused ion beam system (FIB; Carl Zeiss, Germany), and Cs-corrected scanning transmission electron microscopy (Cs-STEM; NEO ARM, JEOL, Japan). The chemical composition was analyzed by energy-dispersive X-ray spectroscopy (EDS), energy-dispersive X-ray fluorescence (XRF; ARL QUANTX, Thermo Fisher Scientific, USA), and X-ray photoelectron spectroscopy (XPS; Nexsa, Thermo Fisher Scientific, USA). The crystallographic properties were evaluated using X-ray

Table 1. Ti and Zn concentrations via XRF analysis

Element	BTS	TZ	TZ-NL
Ti (μg/cm²)	0.157 ± 0.042	0.321 ± 0.036	0.251 ± 0.026
Zn (μg/cm²)	0.103 ± 0.060	0.941 ± 0.068	1.260 ± 0.069

XRF: X-ray fluorescence; BTS: $Bi_2Te_3Se_{0.3}$; TZ-NL: TiO_2/ZnO nanolaminate.

diffraction (XRD; D8 Advance, Bruker, Germany) and fast Fourier transform (FFT; Digital Micrograph, Gatan, Inc., USA). The electrical properties were measured using a Hall measurement system (HMS-3000, Ecopia, Korea), whereas the thermal conductivity and specific heat were evaluated using a laser flash analyzer (LFA; LFA447, NETZSCH, Germany). Electrical conductivity and Seebeck coefficient were measured using a ZEM-3 system (M8, Ulvac, Japan) to assess the overall TE performance.

RESULTS AND DISCUSSION

ZnO-TiO_2 thin film coating and structural/chemical characterization

ZnO and TiO_2 thin films with controlled structures and thicknesses were deposited using ALD. As previously mentioned, the samples with a ZnO/TiO_2/BTS configuration were labeled as TZ, whereas those with a ZnO/TiO_2/ZnO/TiO_2/BTS configuration were labeled as TZ-NL. The target thickness of each layer was set to 2 nm for the TZ and 1 nm for the TZ-NL samples. To quantitatively verify the thin-film deposition, Energy dispersive (ED)-XRF analysis was conducted, and the results are presented in Table 1. Because ED-XRF randomly selects the measurement positions, slight deviations may occur. Thus, measurements were taken at multiple locations, and the average concentrations were reported to represent the overall powder. For raw BTS powders, Ti and Zn concentrations were 0.157 ± 0.042 and 0.103 ± 0.060 μg/cm², respectively, considered as background noise. In contrast, the TZ sample exhibited 0.321 ± 0.036 μg/cm² Ti and 0.941 ± 0.068 μg/cm² Zn, indicating a significant increase and confirming successful film deposition. Similarly, the TZ-NL sample showed 0.251 ± 0.026 μg/cm² Ti and 1.260 ± 0.069 μg/cm² Zn, demonstrating a meaningful enhancement and consistent coating across samples. Although the same thickness of 4 nm was targeted for the coating layer, variations in the GPC depending on the surface could affect the actual film thickness. Specifically, a lower GPC of TiO_2 is expected on the ZnO surface, whereas an enhanced GPC of ZnO is expected on the TiO_2 surface.

To observe the surface morphology changes before and after deposition, HR-FESEM analysis was performed, as shown in Figure 2A-I, which shows low- and high-magnification images (5,000× and 30,000×) and the EDS results of the samples. All samples exhibited irregular particles of similar sizes regardless of the coating layer, indicating no significant change in particle size. At higher magnifications in Figure 2D-F, the plate-like anisotropic morphology of typical BTS remained observable in both TZ and TZ-NL, suggesting that particle collisions during the ALD process did not significantly damage the powder surface inside the rotary reactor.

The EDS analysis results in Figure 2G-I confirm the presence of Ti and Zn in the TZ and TZ-NL samples, which were not detected in the BTS. Though thin films contributed a small fraction of the overall composition, Ti and Zn were detected at approximately 0.1-0.25 at%. Additionally, oxygen content increased from 28.9 at% in BTS to 36.5 at% in TZ and 31.0 at% in TZ-NL, reflecting both film deposition and preexisting surface oxidation. To complement the localized SEM observations, a particle size analysis of Figure 2J was performed. The D_{10}, D_{50}, and D_{90} values (cumulative particle sizes below which 10%, 50%, and 90% of the particles fell) are listed in Table 2. D_{50} was 2.25 μm for BTS, 2.22 μm for TZ, and 2.16 μm for TZ-NL, confirming minimal change in average size post-deposition. The D_{10} and D_{90} values exhibited similar trends. These results indicated that particle agglomeration, often observed in powder ALD with rotary reactors, was effectively suppressed, enabling uniform thin-film deposition[38].

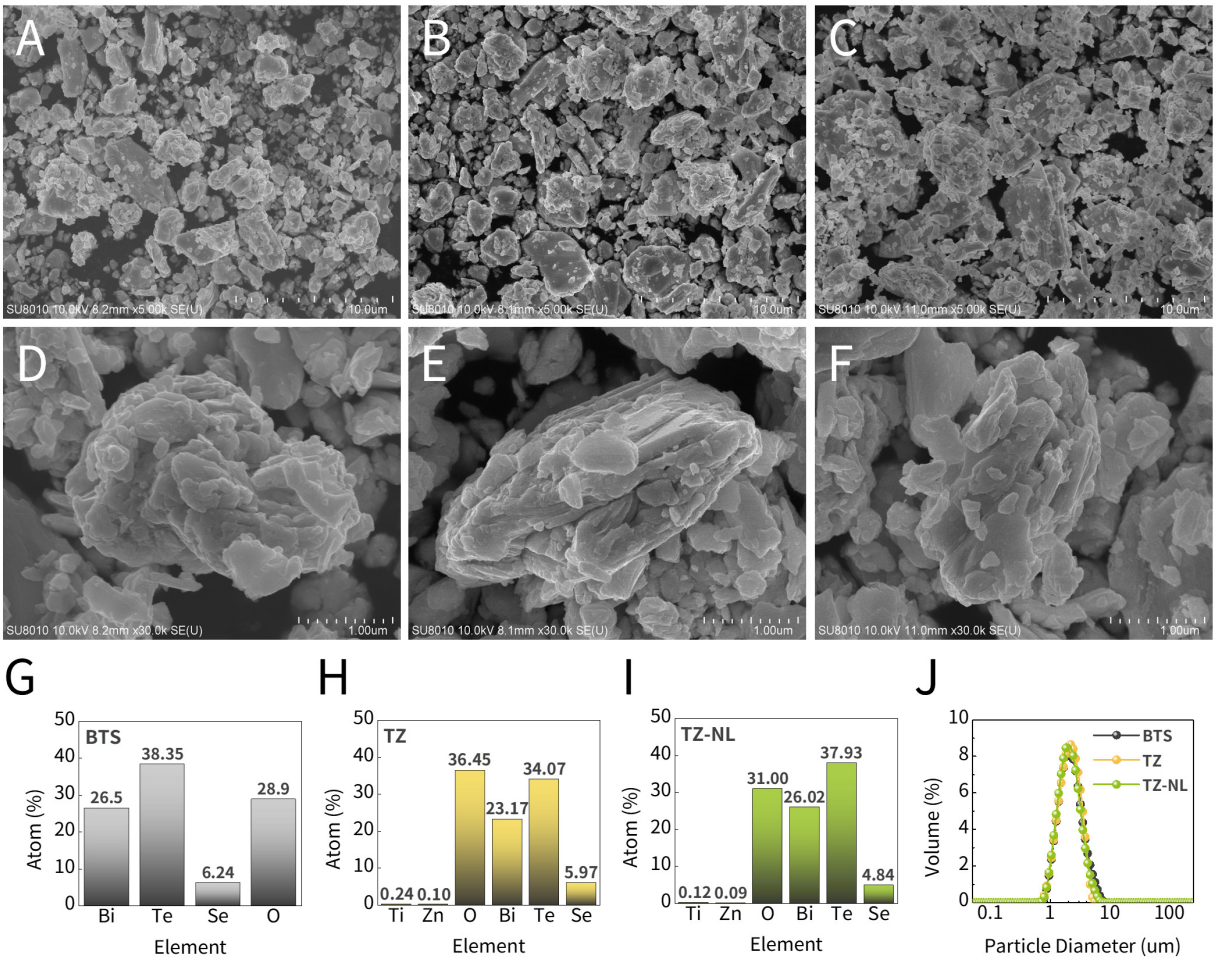

Figure 2. (A-F) HR-FESEM images and (G-I) EDS quantitative analysis for (A, D, G) BTS, (B, E, H) TZ, and (C, F, I) TZ-NL. (J) Particle size distribution. HR-FESEM: High-resolution field-emission scanning electron microscopy; EDS: energy-dispersive X-ray spectroscopy; BTS: $Bi_2Te_3Se_{0.3}$; TZ-NL: TiO_2/ZnO nanolaminate.

Table 2. D_{10}, D_{50}, and D_{90} values for particle size analysis

Sample	BTS	TZ	TZ-NL
D_{10} (μm)	1.31	1.29	1.28
D_{50} (μm)	2.25	2.22	2.16
D_{90} (μm)	4.10	3.66	3.76

BTS: $Bi_2Te_3Se_{0.3}$; TZ-NL: TiO_2/ZnO nanolaminate.

The XPS spectra of Ti 2p, Zn 2p, O 1s, Bi 4f, Te 3d, and Se 3d are shown in Figure 3. As shown in Figure 3A, the Ti $2p_{1/2}$ peak overlapped with that of Bi $4d_{3/2}$, making it difficult to resolve. However, a distinct Ti $2p_{3/2}$ signal was observed near 458 eV in TZ and TZ-NL but not in BTS, indicating successful Ti incorporation. The Ti $2p_{3/2}$ peak was deconvoluted into Ti^{4+} and Ti^{3+} components, with Ti^{4+} being more prominent in TZ and Ti^{3+} being more prominent in TZ-NL. Similarly, Figure 3B showed Zn $2p_{1/2}$ and Zn $2p_{3/2}$ peaks clearly in TZ and TZ-NL, but absent in BTS. These peaks correspond to the Zn^{2+} state, and their intensity increased in TZ-NL compared to TZ. Figure 3C presents the O 1s spectra. The metal-oxygen (M-O) bonding at 529.5-530.2 eV reflects the overlapping signals from Zn-O, Ti-O, Bi-O, and Te-O bonds. Oxygen-vacancy-related components increased after ALD and were higher in TZ-NL than in TZ. Together with the increase in Ti^{3+} observed in Figure 3A, this indicates that more oxygen vacancies were formed in

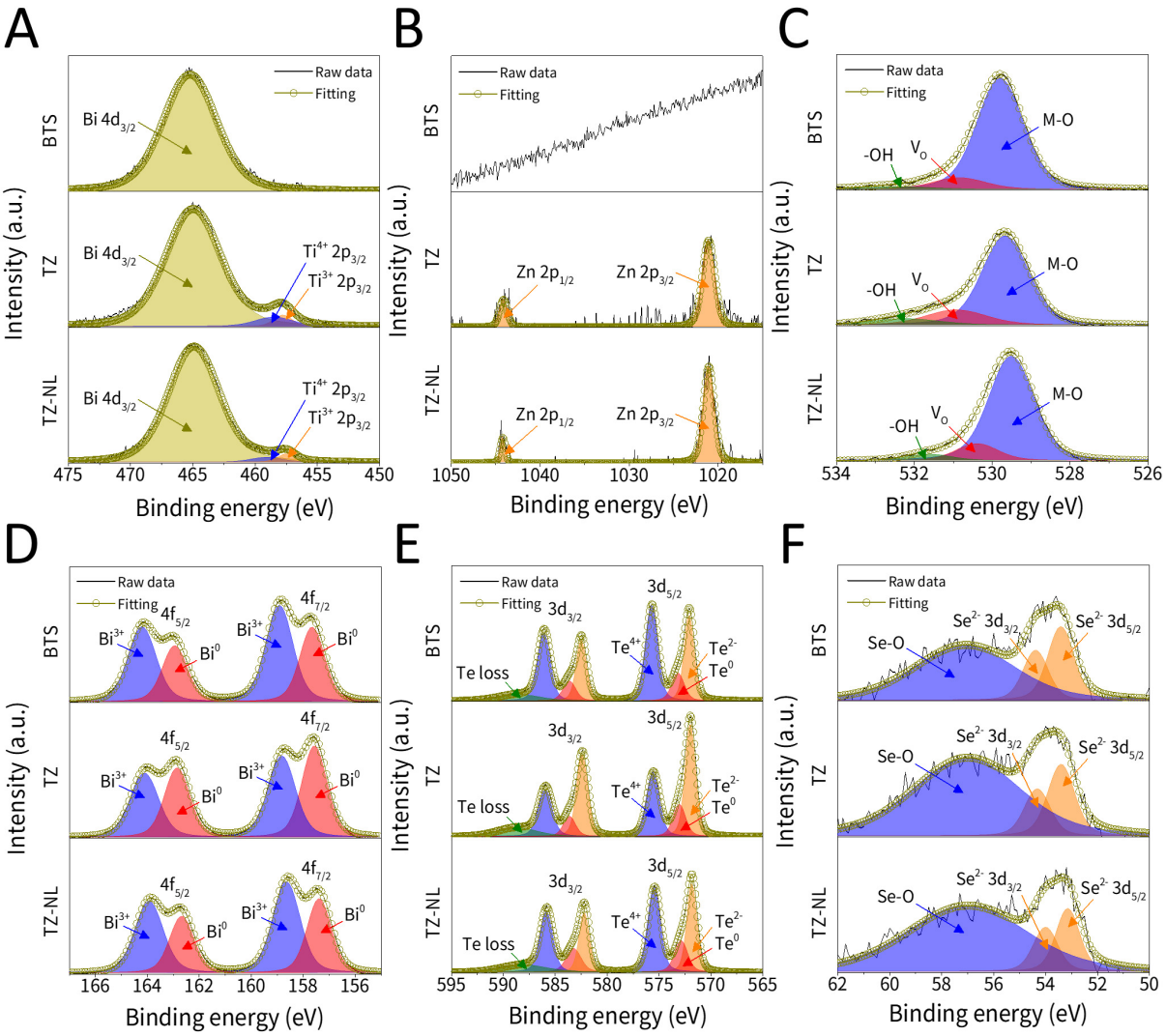

Figure 3. XPS spectra of (A) Ti 2p, (B) Zn 2p, (C) O 1s, (D) Bi 4f, (E) Te 3d, and (F) Se 3d. XPS: X-ray photoelectron spectroscopy; BTS: $Bi_2Te_3Se_{0.3}$; TZ-NL: TiO_2/ZnO nanolaminate.

TZ-NL originating from the ultrathin TiO_2 layer. The OH-related high binding energy component remained at a low level even after ALD, reflecting the low concentration of hydroxyl residues in the ALD-grown oxide films[49]. In Figure 3D-F, Bi^{3+}, Te^{4+}, and Se^{4+} peaks corresponding to Bi-O, Te-O, and Se-O bonds arising from native oxidation and oxide coating were observed alongside the characteristic signals of the BTS matrix. These M-O peaks were more pronounced in TZ-NL than in TZ, suggesting that TZ-NL structure facilitated greater Ti and Zn diffusion into the BTS and promoted active oxygen interactions between the layers, thereby favoring the formation of metal oxides. Notably, an overall shift toward lower binding energy was observed, which shows charge-compensation and doping effects introduced via ALD.

Cross-sectional samples of the TZ and TZ-NL powders were prepared via FIB for Cs-STEM and FFT analyses, as shown in Figure 4A-I. Figure 4B shows a magnified view of the powder surface of the TZ sample shown in Figure 4A, while Figure 4D presents a magnified view of the TZ-NL sample surface shown in Figure 4C. Figure 4B and D both revealed approximately 4-nm-thick amorphous oxide layers formed on the powder. Because of the thin and amorphous phases of the films, the individual TiO_2 and ZnO layers and interfaces could not be resolved. FFT patterns confirmed the amorphous phase of the coating layers. Ti, Zn,and O signals were detected in the coated area via EDS mapping of Figure 4E-H, which corresponds to

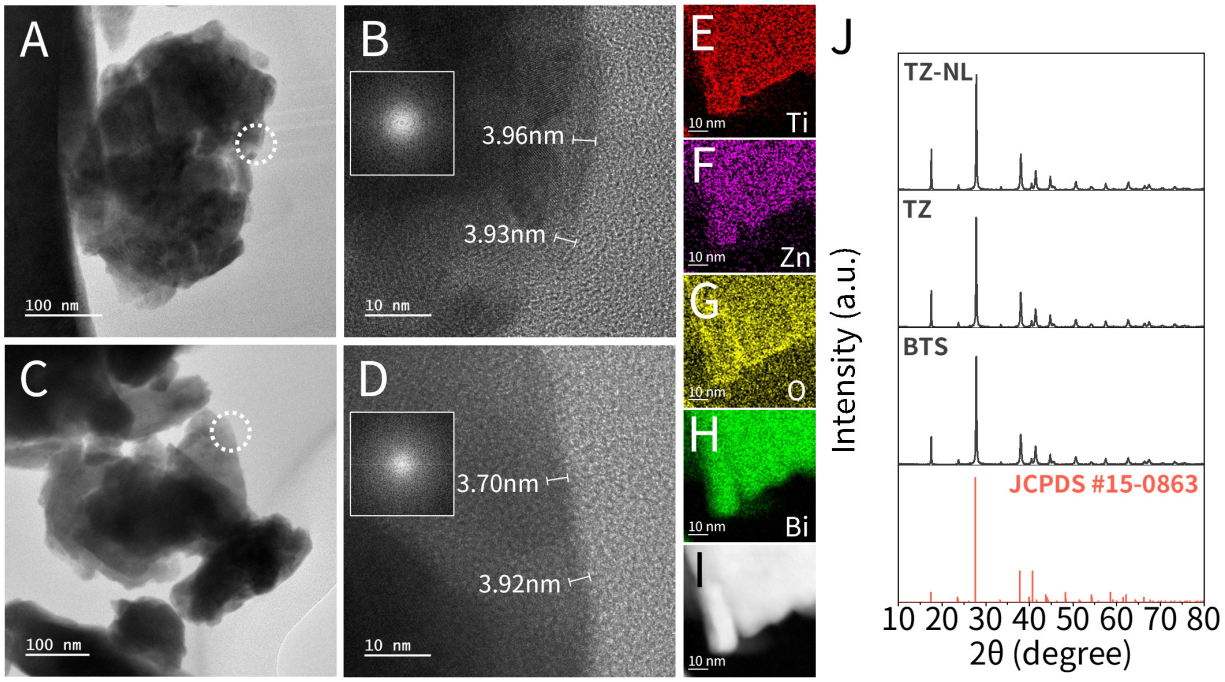

Figure 4. (A-I) Cs-STEM analysis; HRTEM images and thin film FFT patterns of (A and B) TZ and (C and D) TZ-NL powders, (E-H) EDS mapping, and (I) HAADF-STEM image of TZ; (J) XRD spectra. Cs-STEM: Cs-corrected scanning transmission electron microscopy; FFT: fast Fourier transform; EDS: energy-dispersive X-ray spectroscopy; XRD: X-ray diffraction; BTS: $Bi_2Te_3Se_{0.3}$; HRTEM: high-resolution transmission electron microscopy; TZ-NL: TiO_2/ZnO nanolaminate; HAADF-STEM: high-angle annular dark-field scanning transmission electron microscopy.

the high-angle annular dark-field (HAADF) image in Figure 4I, and these signals are clearly distinguishable from the Bi signal in the BTS matrix powders. To further systematically evaluate the crystallinity of the thin film and crosscheck the phase observed in the FFT, XRD analysis was conducted, as shown in Figure 4J. It presents diffraction peaks matching the JCPDS #15-0863 pattern of Bi_2Te_3. No crystalline peaks corresponding to TiO_2 or ZnO are detected, indicating that the films remain amorphous. This result agrees with the FFT observations and confirms that the overall phase of the ALD films is amorphous. Such amorphous structures are beneficial for the TE performance because they increase phonon scattering and reduce the lattice thermal conductivity.

Sintering the multilayer-coated powders

BTS powders coated with TiO_2-ZnO thin films were sintered into pellets using SPS. SPS is a rapid densification technique in which the simultaneous application of high temperature, pressure, and a pulsed direct current (DC) current induces localized heating at the particle contacts owing to resistive heating and plasma generation, thereby enabling fast sintering. In this study, the sintering was performed at 673 K and 50 MPa for 5 min. The resulting pellets exhibited a relative density of over 95%, which was sufficient to prevent electrical conductivity degradation due to porosity and to ensure mechanical reliability. To observe the microstructure after sintering, cross-sectional pellets were prepared via FIB and analyzed using Cs-STEM. The results are shown in Figure 5. Figure 5A-C show the coated region of a TZ sample, its corresponding FFT pattern, and its atomic concentration via EDS quantitative analysis, whereas Figure 5D-F present the data for the TZ-NL sample. An amorphous layer approximately 4 nm thick was observed at the interface between the highly crystallized BTS grains. During sintering, the two coating layers did not merge to form an interface twice the thickness of the individual coatings; instead, a uniform ~4 nm interface was consistently present. This behavior is attributed not only to densification during SPS but also to the shadowing effect in the ALD process. Although ALD typically ensures high coating uniformity, the

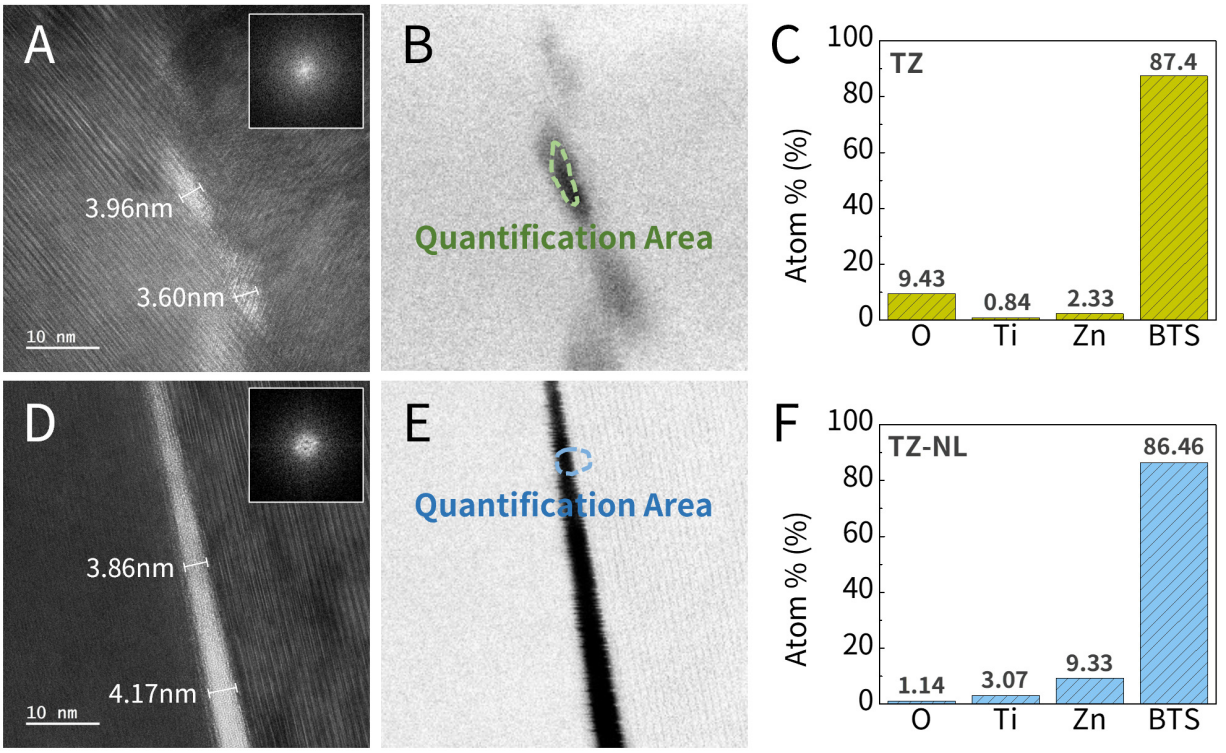

Figure 5. HRTEM images with thin film FFT pattern and EDS quantification in the marked area of (A-C) TZ and (D-F) TZ-NL. FFT: Fast Fourier transform; EDS: energy-dispersive X-ray spectroscopy; HRTEM: high-resolution transmission electron microscopy; TZ-NL: TiO_2/ZnO nanolaminate.

agglomerated structure of the powders and limited diffusion of the precursors can lead to an incomplete coating in certain regions, resulting in the formation of imperfect interfaces after sintering. Consequently, it was inferred that in both TZ and TZ-NL, the fully and partially coated particles underwent densification to form an interface of approximately 4 nm. However, unlike TZ-NL, in which a continuous interface with a uniform thickness of 4 nm was observed, the bilayer film of TZ was discontinuous. The TZ-NL thin film, in which stable metal-oxide bonding was formed through alternating 1 nm depositions, was relatively well preserved during the sintering process. EDS mapping of this amorphous interfacial layer revealed Ti, Zn, and O contents of 0.84 at%, 2.33 at%, and 9.43 at% for TZ, and 3.07 at%, 9.33 at%, and 1.14 at% for TZ-NL, respectively. Because the atomic ratios of Ti and Zn were extremely low compared with those of the BTS matrix, broad-area compositional analysis lacked sufficient sensitivity; thus, a region-specific analysis was conducted. Both TZ and TZ-NL exhibited a structure in which ZnO was located on the outer surface, and during sintering, the diffusion of Zn into the BTS was more limited than that of Ti, leading to a locally high Zn concentration with a Ti:Zn ratio of approximately 1:3. It was also confirmed that Ti and Zn remained distributed within the localized thin-film regions even after sintering. In the TZ-NL sample, this continuous and stable metal oxide interfacial layer can reduce the density of interfacial defects that act as charge traps, thereby increasing the effective carrier concentration. Furthermore, continuous electron transport pathways are expected to enhance carrier mobility.

Thermoelectric properties

These charge-transport characteristics were further investigated through Hall-effect measurements, as shown in Figure 6. As shown in Figure 6A, the carrier concentration (n_H) increased in both the TZ and TZ-NL pellet samples compared to that in BTS. This can be attributed to the change in the valence state caused by the diffusion of Zn^{2+} into Bi^{3+} sites in Bi_2Te_3. Additionally, the oxygen vacancies generated in ultrathin TiO_2 layers

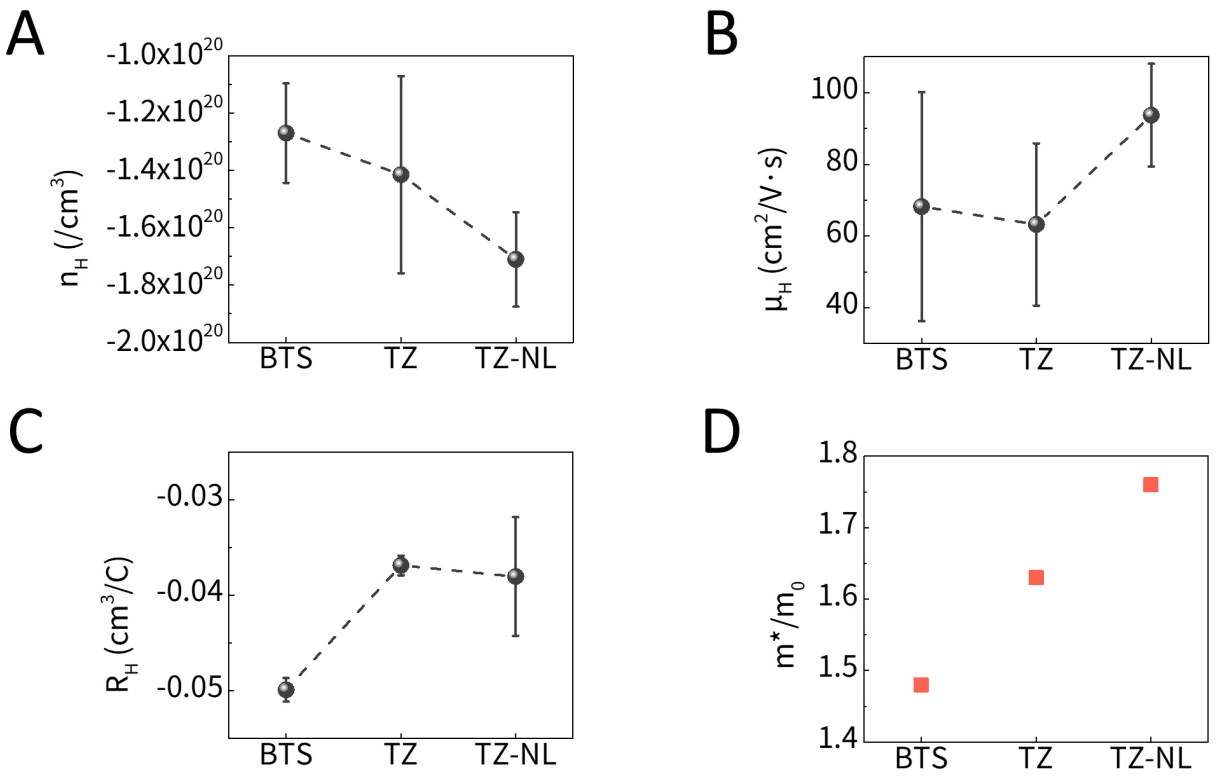

Figure 6. Hall-measurement results; (A) carrier concentration (n_H), (B) carrier mobility (μ_H), (C) average Hall coefficient (R_H) and (D) effective mass(m^*/m_0) calculated from Pisarenko relation. BTS: $Bi_2Te_3Se_{0.3}$; TZ-NL: TiO_2/ZnO nanolaminate.

of approximately 1 nm can also contribute to an increase in the carrier concentration. In particular, the TZ-NL structure exhibited a more pronounced electron-donating effect owing to greater diffusion and higher interface density, resulting in the highest carrier concentration, whereas TZ showed a relatively moderate increase, likely because of dominant electron-blocking effects. This n-type donor effect originating from such substitutional reactions and oxygen vacancies was corroborated by the XPS analysis shown in Figure 3. Figure 6B shows carrier mobility (μ_H), which was also highest in the TZ-NL sample. Each layer of TZ-NL is thinner than the sub-nanometer electron mean free path (MFP), thereby minimizing the degradation in the mobility of high-energy carriers. Figure 6C shows the average Hall coefficient (R_H), which is inversely related to the carrier concentration. Based on Figure 6A, TZ-NL was expected to exhibit a lower R_H than TZ. The actual results showed a slightly higher R_H; however, the difference was negligible, as shown in Figure 6C. Nevertheless, the overall trend remains consistent with the theoretical expectations. Figure 6D shows the effective mass (m^*/m_0) calculated using the Pisarenko equation at 300 K under the assumptions of a single-parabolic-band (SPB) model and dominant acoustic-phonon scattering. The BTS specimen in this study exhibits a higher n_H than that in previous studies due to surface oxidation and partial bipolar conduction; therefore, the m^* of pristine BTS calculated with the SPB model may be overestimated. This should be considered, and further refinement using the Kane or modified band model is recommended for more accurate evaluation[50]. The Pisarenko relation is expressed as follows:

$$S = \frac{8\pi^2 k_B^2 T}{3eh^2} m^* \left(\frac{\pi}{3n}\right)^{2/3} \quad (2)$$

Generally, a larger m^*/m_0 leads to an increased scattering of charge carriers. However, in this study, the dominant contribution of the $n^{2/3}$ term resulting from the strong doping effects in TZ-NL, combined with the optimization of conduction pathways through continuous interfaces, significantly enhanced the carrier mobility and conduction properties. Therefore, despite having a larger m^*/m_0 than those of BTS and TZ, and

exhibiting a reduced energy filtering effect owing to the high carrier concentration, the TZ-NL sample demonstrated superior electrical conduction properties compared to those of BTS.

The TE performance of the (TiO_2-ZnO)/BTS-sintered pellets was further evaluated using LFA and ZEM-3 measurements. The results are shown in Figure 7, including electrical conductivity, Seebeck coefficient, thermal conductivity, power factor, and zT. As shown in Figure 7A, although oxide coatings generally reduce electrical conductivity owing to lattice mismatch and insulating effects, n-type oxides, such as TiO_2 and ZnO, can act as electron donors or dopants. This doping effect is particularly pronounced in the TZ-NL sample, where ultrathin individual layers are alternately deposited, resulting in a significantly higher electrical conductivity compared to BTS. As confirmed in Figure 6A-B, this improvement is closely associated with the high carrier concentration and mobility derived from the stable maintenance of the continuous metal oxide layer. Figure 7B shows the Seebeck coefficient, which is influenced by the energy-filtering effects at the potential barriers formed at the interfaces. As shown in Figure 6D, the TZ-NL specimen exhibits a higher effective mass than BTS, along with band flattening and an increased density of states (DOS), which would generally contribute to an enhanced Seebeck coefficient. However, the donor effects of Zn ions and oxygen vacancies caused a rapid increase in the $n^{2/3}$ term in the Pisarenko relation, which predominantly governed the Seebeck behavior. Consequently, despite the sufficient contribution from DOS enhancement, the high electron concentration weakened the energy-barrier effect, and bulk carrier transport became dominant, leading to the observed suppression of the Seebeck coefficient. In contrast, TZ exhibited a higher Seebeck coefficient than BTS because its carrier concentration and effective mass were appropriately balanced. Figure 7C shows that both coated samples exhibited an improved power factor (PF) compared to BTS. Notably, TZ-NL, benefiting from its high electrical conductivity, reached approximately 2.2 $mW/m{\cdot}K^2$, indicating its superior electron transport characteristics under the multilayer structure. Figure 7D-E present the total thermal conductivity and the sum of the lattice and bipolar contributions, respectively. The partial influence of bipolar conduction was confirmed by Debye-Callaway fitting. The total thermal conductivity decreased after ALD coating relative to that of pristine BTS, which is attributed to enhanced phonon scattering at heterogeneous interfaces. While TZ-NL possesses a higher carrier concentration and therefore a greater contribution from electronic thermal conductivity, TZ exhibited comparatively lower total thermal conductivity. Meanwhile, the ($\kappa_{lat} + \kappa_{bi}$) value was lower in TZ-NL than in TZ, which is interpreted as a consequence of the higher interfacial density and the continuous, stable interfaces in TZ-NL that are preserved even after sintering, leading to an increased probability of phonon scattering. In the case of TZ, the formation of thicker interfaces is expected to strengthen phonon-scattering intensity; however, the bilayer structure and high discontinuity reduce its interfacial density, thereby decreasing the phonon-scattering probability and limiting the reduction in lattice thermal conductivity. Consequently, Figure 7F shows that TZ-NL achieved a zT value of approximately 0.8 at 460 K, representing a 27% improvement over BTS. This indicates that, despite a slightly lower Seebeck coefficient, the higher electrical conductivity and reduced thermal conductivity of the NL structure significantly contributed to the overall performance enhancement.

The effects of the TiO_2-ZnO multilayer coating were comprehensively evaluated by comparing the PF within our research group [Figure 8A] and the maximum zT and PF reported by other groups [Figure 8B]. Single-oxide coatings of 4/6 nm ZnO and 4/8 nm TiO_2 effectively reduced the lattice thermal conductivity; however, the accompanying decrease in electrical conductivity limited the PF improvement, as shown in Figure 8A[38]. In contrast, the TiO_2-ZnO multilayer developed in this study preserved or even enhanced the intrinsic electrical conductivity of pristine BTS, thereby achieving the highest PF. Furthermore, when compared with sub-5 nm single-oxide coatings of Al_2O_3, ZnO, SnO_2, and TiO_2 in Figure 8B, the TiO_2-ZnO multilayer exhibited a moderate increase in zT_{max} but achieved a high PF_{max} of 2.2 $mW/m{\cdot}K^2$[13,14,37,51]. Although oxide-interface engineering typically leads to electrical conductivity loss, the multilayer strategy can overcome this limitation and significantly enhance PF. Advanced strategies, including interface engineering

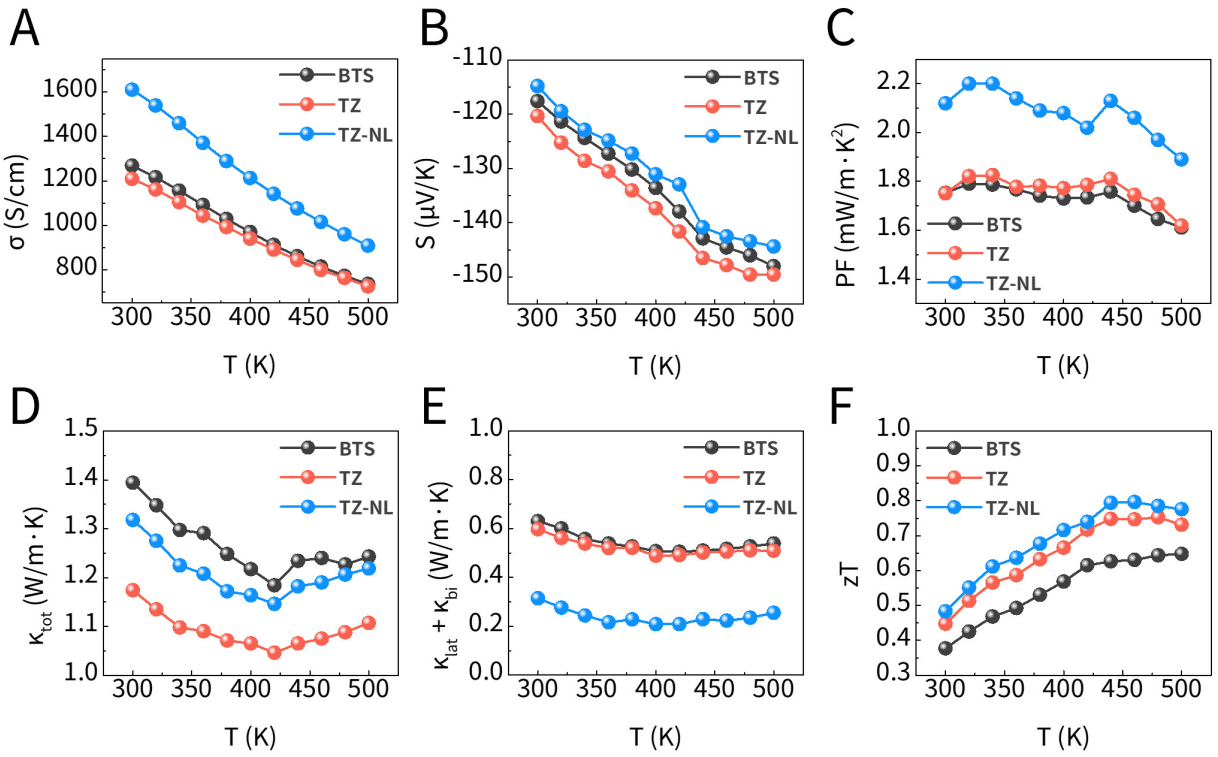

Figure 7. Thermoelectric properties; (A) electrical conductivity (σ), (B) Seebeck coefficient (S), (C) power factor (PF), (D) total thermal conductivity (κ_{tot}), (E) lattice thermal conductivity (κ_{lat}) + bipolar thermal conductivity (κ_{bi}), and (F) zT as a function of temperature. BTS: $Bi_2Te_3Se_{0.3}$; zT: thermoelectric figure of merit; TZ-NL: TiO_2/ZnO nanolaminate.

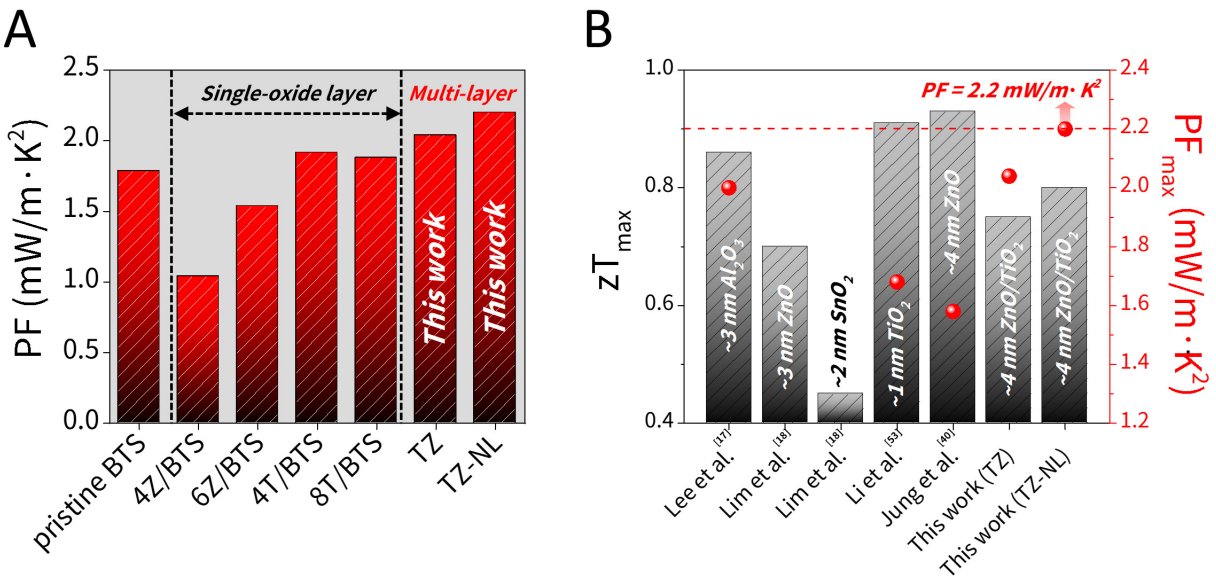

Figure 8. Comparison of (A) power factor (PF) within our research group and (B) maximum values of zT (zT_{max}) and PF (PF_{max}) with those reported by other research groups. BTS: $Bi_2Te_3Se_{0.3}$; thermoelectric figure of merit; TZ-NL: TiO_2/ZnO nanolaminate.

as well as nanoprecipitation and texturing, which can yield zT values exceeding 1.0, have also been reported to maintain or even reduce PF[12,52,53]. Moreover, doping and hot-pressing methods are often sensitive to slight compositional deviations and have instability of doping profiles and microstructures during prolonged high-temperature exposure[54-56]. In this context, ALD provides atomic-precision control over both thickness and composition, minimizing sample-to-sample variation and forming robust chemical bonding. Consequently, ALD-SPS integration effectively suppresses compositional loss, underscoring its strong potential as a high-performance and reliable TE material fabrication platform.

CONCLUSIONS

In this study, TiO_2-ZnO oxide films were conformally coated onto Bi_2Te_3-based powders via ALD, followed by consolidation into dense pellets via SPS. The structural and chemical stabilities of the resulting interfaces, along with their impact on the TE performance, were systematically evaluated. Powders coated with either a 2/2 nm bilayer (TZ) or a 1/1/1/1 nm multilayer structure (TZ-NL) retained approximately 4 nm amorphous interfacial layers, even after high-density sintering, as confirmed by high-resolution transmission electron microscopy (HR-TEM) and EDS analysis. TZ sample exhibited an increased Seebeck coefficient with the balanced carrier concentration and effective mass in heterogeneous films. Notably, the TZ-NL structure exhibited enhanced carrier concentration and mobility owing to electron donation and diffusion doping at multiple interfaces, which contributed significantly to the recovery of electrical conductivity. In addition, high interfacial density and continuous films effectively induce phonon scattering, lowering lattice thermal conductivity. These improvements led to a zT of 0.8 at 460 K in the TZ-NL sample, achieving a 27% improvement compared to the uncoated BTS. These findings demonstrate that interfacial engineering using ALD-grown multilayer oxide films can effectively modulate the charge- and phonon-transport properties of TE materials. This highlights the potential of complex oxide interface design as a viable strategy for enhancing TE performance.

DECLARATIONS

Authors' contributions

Data collection: Eun, S. M.; Shin, J. K.
Study design, data analysis, and original manuscript writing: Eun, S. M.
Supervision and manuscript revision suggestions: Choi, B. J.
Technical and material support: Lee, E. S.; Oh, S. T.

Availability of data and materials

The data that support the findings of this study are available from the corresponding author upon reasonable request.

AI and AI-assisted tools statement

Not applicable.

Financial support and sponsorship

This work was supported by the National Research Foundation of Korea (NRF) grant funded by the Korean Government (MSIT) (NRF-2023R1A2C1006831).

Conflicts of interest

All authors declared that there are no conflicts of interest.

Ethical approval and consent to participate

Not applicable.

Consent for publication

Not applicable.

REFERENCES

1. D'angelo, M.; Galassi, C.; Lecis, N. Thermoelectric materials and applications: a review. *Energies* **2023**, *16*, 6409. DOI
2. Massetti, M.; Jiao, F.; Ferguson, A. J.; et al. Unconventional thermoelectric materials for energy harvesting and sensing applications. *Chem. Rev.* **2021**, *121*, 12465-547. DOI PubMed

3. Finn, P. A.; Asker, C.; Wan, K.; Bilotti, E.; Fenwick, O.; Nielsen, C. B. Thermoelectric materials: current status and future challenges. *Front. Electron. Mater.* **2021**, *1*, 677845. DOI
4. Zafar, M. H.; Khan, N. M.; Mansoor, M.; Khan, U. A. Towards green energy for sustainable development: machine learning based MPPT approach for thermoelectric generator. *J. Clean. Prod.* **2022**, *351*, 131591. DOI
5. Champier, D. Thermoelectric generators: a review of applications. *Energy. Convers. Manag.* **2017**, *140*, 167-81. DOI
6. Bu, Z.; Zhang, X.; Hu, Y.; et al. A record thermoelectric efficiency in tellurium-free modules for low-grade waste heat recovery. *Nat. Commun.* **2022**, *13*, 237. DOI PubMed PMC
7. Zhu, T.; Liu, Y.; Fu, C.; Heremans, J. P.; Snyder, J. G.; Zhao, X. Compromise and synergy in high-efficiency thermoelectric materials. *Adv. Mater.* **2017**, *29*, 1605884. DOI
8. Okirigiti, M. A.; Kim, C. M.; Choi, H.; Alluri, N. R.; Park, K. Recent advances in thermoelectric materials and devices: improving power generation performance. *J. Powder. Mater.* **2025**, *32*, 1-15. DOI
9. Bae, J.; Jo, S.; Kim, K. T. Enhancing electrical properties of N-type bismuth telluride alloys through graphene oxide incorporation in extrusion 3D printing. *J. Powder. Mater.* **2023**, *30*, 318-23. DOI
10. Lee, S.; Park, T. J.; Kim, S. K. Recent progress on performance improvements of thermoelectric materials using atomic layer deposition. *J. Powder. Mater.* **2022**, *29*, 56-62. DOI
11. Lee, S.; Jung, S.; Park, G. M.; et al. Grain boundary engineering strategy for simultaneously reducing the electron concentration and lattice thermal conductivity in n-type $Bi_2Te_{2.7}Se_{0.3}$-based thermoelectric materials. *J. Eur. Ceram. Soc.* **2023**, *43*, 3376-82. DOI
12. Lim, S.; Kim, K.; Lee, S.; et al. Carrier Modulation in Bi_2Te_3-based alloys via interfacial doping with atomic layer deposition. *Coatings* **2020**, *10*, 572. DOI
13. Lee, S.; Park, G. M.; Kim, Y.; et al. Unlocking the potential of porous Bi_2Te_3-based thermoelectrics using precise interface engineering through atomic layer deposition. *ACS. Appl. Mater. Interfaces.* **2024**, *16*, 17683-91. DOI PubMed
14. Park, K. H.; Mohamed, M.; Aksamija, Z.; Ravaioli, U. Phonon scattering due to van der Waals forces in the lattice thermal conductivity of Bi_2Te_3 thin films. *J. Appl. Phys.* **2015**, *117*, 015103. DOI
15. Fang, T.; Li, X.; Hu, C.; et al. Complex band structures and lattice dynamics of Bi_2Te_3-based compounds and solid solutions. *Adv. Funct. Mater.* **2019**, *29*, 1900677. DOI
16. Li, C.; Zhou, Z.; Lou, Y.; Fu, L. Lattice softening in thermoelectric materials. *Microstructures* **2025**, *5*, 2025075. DOI
17. Dharmaiah, P.; Jung, S.; Kim, J.; Kim, S. K.; Baek, S. Why is it challenging to improve the thermoelectric properties of *n*-type Bi_2Te_3 alloys? *Appl. Phys. Rev.* **2024**, *11*, 031312. DOI
18. Irfan, S.; Yan, Z.; Khan, S. B. Advancements in thermoelectric materials: a comprehensive review. *Mater. Sci. Energy. Technol.* **2024**, *7*, 349-73. DOI
19. Theja, V. C. S.; Karthikeyan, V.; Assi, D. S.; Roy, V. A. L. Insights into the classification of nanoinclusions of composites for thermoelectric applications. *ACS. Appl. Electron. Mater.* **2022**, *4*, 4781-96. DOI
20. Lu, X.; Pan, G.; Shi, Z.; Xu, B.; Lou, Y. Recent advances in interface engineering of thermoelectric nanomaterials. *Mater. Chem. Front.* **2023**, *7*, 4707-22. DOI
21. Li, S.; Wang, L.; Ma, D.; Jiang, Y.; Guo, K.; Luo, J. Recent advances in atomic layer deposition-based interface modification engineering in thermoelectric materials. *Mater. Today. Phys.* **2023**, *39*, 101287. DOI
22. Kim, K. C.; Lim, S. S.; Lee, S. H.; et al. Precision interface engineering of an atomic layer in bulk Bi_2Te_3 alloys for high thermoelectric performance. *ACS. Nano.* **2019**, *13*, 7146-54. DOI
23. He, S.; Bahrami, A.; Zhang, X.; Martínez, I. G.; Lehmann, S.; Nielsch, K. Effect of powder ALD interface modification on the thermoelectric performance of bismuth. *Adv. Mater. Technol.* **2021**, *7*, 2100953. DOI
24. Park, G. M.; Lee, S.; Park, T. J.; Baek, S. H.; Kim, J. S.; Kim, S. K. Controlled engineering of defects and interfaces in thermoelectric materials with atomic layer deposition. *Adv. Mater. Interfaces.* **2024**, *12*, 2400581. DOI
25. George, S. M. Atomic layer deposition: an overview. *Chem. Rev.* **2010**, *110*, 111-31. DOI PubMed
26. Liu, W.; Hu, J.; Zhang, S.; Deng, M.; Han, C.; Liu, Y. New trends, strategies and opportunities in thermoelectric materials: a perspective. *Mater. Today. Phys.* **2017**, *1*, 50-60. DOI
27. Jung, C.; Jeon, S.; Lee, S.; et al. Reduced lattice thermal conductivity through tailoring of the crystallization behavior of NbCoSn by V addition. *J. Alloys. Compd.* **2023**, *962*, 171191. DOI
28. Bueno Villoro, R.; Zavanelli, D.; Jung, C.; et al. Grain boundary phases in NbFeSb half-heusler alloys: a new avenue to tune transport properties of thermoelectric materials. *Adv. Energy. Mater.* **2023**, *13*, 2204321. DOI
29. Pei, Y.; Wang, H.; Snyder, G. J. Band engineering of thermoelectric materials. *Adv. Mater.* **2012**, *24*, 6125-35. DOI
30. Venkatasubramanian, R.; Siivola, E.; Colpitts, T.; O'Quinn, B. Thin-film thermoelectric devices with high room-temperature figures of merit. *Nature* **2001**, *413*, 597-602. DOI PubMed

31. Bueno Villoro, R.; Hatami Naderloo, R.; Mattlat, D. A.; et al. Composite design of half-Heusler thermoelectrics: selective doping of grain boundary phases in NbFeSb by InSb. *Mater. Today. Phys.* **2023**, *38*, 101240. DOI
32. Zheng Y, ; Slade TJ, ; Hu L, ; et al. Defect engineering in thermoelectric materials: what have we learned? *Chem. Soc. Rev.* **2021**, *50*, 9022-54. DOI PubMed
33. Jung, C.; Dutta, B.; Dey, P.; et al. Tailoring nanostructured NbCoSn-based thermoelectric materials via crystallization of an amorphous precursor. *Nano. Energy.* **2021**, *80*, 105518. DOI
34. Zhang, Y.; Peng, G.; Li, S.; et al. Phase interface engineering enables state-of-the-art half-Heusler thermoelectrics. *Nat. Commun.* **2024**, *15*, 5978. DOI PubMed PMC
35. Luo, Y.; Zhu, J.; Rao, X.; et al. Optimized interface engineering enhances carrier and phonon scattering for superior thermoelectric performance in Yb-filled skutterudites. *ACS. Appl. Mater. Interfaces.* **2025**, *17*, 8047-54. DOI PubMed
36. Santhosh, R.; Kamalakannan, S.; Harish, S.; Archana, J.; Ponnusamy, S.; Navaneethan, M. Interface-driven energy filtering effect and enhanced thermoelectric performance of Ag_2Se/SnS composites: an experimental and theoretical insights. *J. Colloid. Interface. Sci.* **2025**, *691*, 137375. DOI
37. He, S.; Bahrami, A.; Jung, C.; et al. Precision interface engineering of CuNi alloys by powder ALD toward better thermoelectric performance. *Adv. Funct. Mater.* **2024**, *34*, 2314457. DOI
38. Jung, M. J.; Ji, M.; Han, J. H.; et al. Atomic layer deposition of ZnO layers on Bi_2Te_3 powders: comparison of gas fluidization and rotary reactors. *Ceram. Int.* **2022**, *48*, 36773-80. DOI
39. Jung, M. J.; Park, J. Y.; Eun, S. M.; Choi, B. J. Thermoelectric performance enhancement of sintered Bi-Te Pellets by rotary-type atomic layer deposition. *J. Powder. Mater.* **2023**, *30*, 130-9. DOI
40. Yang, J.; Daqiqshirazi, M.; Ritschel, T.; et al. Interfacial distortion of Sb_2Te_3-Sb_2Se_3 multilayers via atomic layer deposition for enhanced thermoelectric properties. *ACS. Nano.* **2024**, *18*, 17500-8. DOI
41. Rawther, A. N.; Rout, U.; S, P. K. D.; Ramanathan, R.; Mallik, R. C. Thermoelectric properties of sputter deposited Bi_2Te_3-PbTe multilayer thin films. *Phys. B. Condens. Matter.* **2024**, *673*, 415467. DOI
42. Wang, G.; Meng, F.; Chen, Y.; Lotnyk, A.; Shen, X. Boosting thermoelectric performance of Bi_2Te_3 material by microstructure engineering. *Adv. Sci.* **2024**, *11*, e2308056. DOI PubMed PMC
43. Kong, F.; Bai, J.; Zhao, Y.; et al. Ultralow thermal conductivity and high thermoelectric performance of Cu_2Se/TiO_2 nanocomposite. *Appl. Phys. Lett.* **2019**, *115*, 203901. DOI
44. Liu, C.; Miao, L.; Zhou, J.; Huang, R.; Fisher, C. A. J.; Tanemura, S. Chemical tuning of TiO_2 nanoparticles and sintered compacts for enhanced thermoelectric properties. *J. Phys. Chem. C.* **2013**, *117*, 11487-97. DOI
45. Liu, H.; Ma, H.; Su, T.; et al. High-thermoelectric performance of TiO_{2-x} fabricated under high pressure at high temperatures. *J. Materiomics.* **2017**, *3*, 286-92. DOI
46. Liu, X.; Kepaptsoglou, D.; Gao, Z.; et al. Controlling the thermoelectric properties of Nb-doped TiO_2 ceramics through engineering defect structures. *ACS. Appl. Mater. Interfaces.* **2021**, *13*, 57326-40. DOI PubMed
47. Tsubota, T.; Ohtaki, M.; Eguchi, K.; Arai, H. Thermoelectric properties of Al-doped ZnO as a promising oxide material for high-temperature thermoelectric conversion. *J. Mater. Chem.* **1997**, *7*, 85-90. DOI
48. Jayaseelan, V.; Mani, N.; Eswaran, S. K. Large electrical conductivity and thermoelectric power factor of pulsed laser-deposited Zn_xGa_xO thin films. *ACS. Appl. Energy. Mater.* **2024**, *7*, 1693-9. DOI
49. Bakos, L. P.; Justh, N. Moura da Silva Bezerra da Costa, U. C.; et al. Photocatalytic and gas sensitive multiwalled carbon nanotube/TiO_2-ZnO and ZnO-TiO_2 composites prepared by atomic layer deposition. *Nanomaterials* **2020**, *10*, 252. DOI
50. Wang, H.; Gurunathan, R.; Fu, C.; Cui, R.; Zhu, T.; Snyder, G. J. Thermoelectric transport effects beyond single parabolic band and acoustic phonon scattering. *Mater. Adv.* **2022**, *3*, 734-55. DOI
51. Li S, ; Chu M, ; Zhu W, ; et al. Atomic-scale tuning of oxygen-doped $Bi_2Te_{2.7}Se_{0.3}$ to simultaneously enhance the Seebeck coefficient and electrical conductivity. *Nanoscale* **2020**, *12*, 1580-8. DOI PubMed
52. Li, D.; Li, J. M.; Li, J. C.; et al. High thermoelectric performance of n-type $Bi_2Te_{2.7}Se_{0.3}$ *via* nanostructure engineering. *J. Mater. Chem. A.* **2018**, *6*, 9642-9. DOI
53. Liu, Y.; Zhang, Y.; Lim, K. H.; et al. High thermoelectric performance in crystallographically textured n-type $Bi_2Te_{3-x}Se_x$ produced from asymmetric colloidal nanocrystals. *ACS. Nano.* **2018**, *12*, 7174-84. DOI
54. Kim, G.; Lee, K.; Shin, H.; et al. Strong enhancement of room-temperature thermoelectric properties of Cu-doped $Bi_2Te_{2.7}Se_{0.3}$. *Appl. Phys. Lett.* **2022**, *120*, 043903. DOI
55. Li, Q.; Wei, Z.; Ma, Q.; Li, Z.; Luo, J. Optimizing room-temperature thermoelectric performance of n-type $Bi_2Te_{2.7}Se_{0.3}$. *ACS. Omega.* **2021**, *6*, 33883-8. DOI PubMed PMC

56. Chen, T.; Li, S.; Chen, K.; et al. Enhancing thermoelectric performance of n-type $Bi_2Te_{2.7}Se_{0.3}$ through Incorporation of amorphous Si_3N_4 nanoparticles. *ACS. Appl. Mater. Interfaces.* **2024**, *16*, 22016-24. DOI PubMed